https://doi.org/10.52131/jmps.2022.0301.0021

Journal of Materials and Physical Sciences

Volume 3, Number 1, 2022, Pages 01 - 13

Journal Homepage:
https://journals.internationalrasd.org/index.php/jmps

JOURNAL OF MATERIALS AND PHYSICAL SCIENCES
INTERNATIONAL RESEARCH ASSOCIATION FOR SUSTAINABLE DEVELOPMENT

Tuning the Properties of Praseodymium Cobalt-Zinc Ferrites by Substitution of Bismuth

Ruba Akbar[1], Muhammad Shahzad Shifa[2*], Aamir Saleem[2], Aurang Zaib[2], Faseeh ur Raheem[2], Muhammad Waqas Khaliq[3*]

[1] Department of Physics, Government College University, Faisalabad, Pakistan
[2] Institute of Physics, The Islamia University of Bahawalpur, Bahawalpur, 63100, Pakistan
[2] ALBA Synchrotron Light Source, Carrer de la Llum, 2, 26, 08290 Cerdanyola del Vallès, Barcelona, Spain

ARTICLE INFO

Article History:
Received: January 20, 2022
Revised: March 19, 2022
Accepted: June 28, 2022
Available Online: June 29, 2022

Keywords:
Bismuth Ferrite
X-Ray Diffraction
Scanning Electron Microscope
UV-Visible Spectroscopy
Fourier Transform IR Spectroscopy

ABSTRACT

This work carried out the study of $Co_{0.5}Zn_{0.5}Bi_{0.4-x}Pr_{0.1}Fe_{1.5+x}O_4$ spinel ferrite series (x = 0,0.1, 0.2, 0.3 and 0.4) prepared via micro-emulsion route. Effects on structural, electrical, optical and morphology properties is studied by varying Bi concentration (x = 0,0.1, 0.2, 0.3 and 0.4). The characterization techniques employed included X-ray diffraction (XRD), scanning electron microscope (SEM), UV-visible spectroscopy and Fourier transform infrared spectroscopy (FTIR). XRD results confirmed the spinel structure having lattice parameter around 8.39 Å and particle size decreased from 30 nm to 41 nm with increasing Bi concentration. Fourier transform infrared spectroscopy (FTIR) revealed fingerprints of metal oxides band at 408-577 cm^{-1}. Optical properties were studied UV-visible spectroscopy and Eg was found to vary from 2.83 eV to 2.59 eV. The scanning electron microscope (SEM) described the morphology of the samples. We then examine the results and the material's characteristics, as well as the areas in which it can be used.

*Corresponding Authors' Email: shahzad.shifa@iub.edu.pk, mkhaliq@cells.es

1. Introduction

Spinel ferrites are the most researched ferrimagnetic materials which are finding its applications in emerging material sciences. (Batoo et al., 2022) These ferrites have cubic FCC structure having at least a divalent meal ion in addition to iron oxide. The metal ion is replaced by combinations of two or more different ions to optimize the ferrite's structure in order to obtain the desired properties. (Velhal, Patil, Shelke, Deshpande, & Puri, 2015) Cobalt is progressively reported to increase the magnetic properties of soft spinel ferrites due its magnetic nature and light weight. (Almuhamady & Aboulfotoh, 2012) Cobalt's higher cost hinders its substitution in larger amounts in ferrites. To circumvent this problem and for a cost-effective preparation it is wise to try a combination of this element with another divalent metal ion. Zinc is another divalent metal atom but it does not affect the magnetic properties due to its diamagnetic nature. (Velhal et al., 2015) However combination of Cobalt and Zinc is very promising and it is finding numerous applications in fast switching (Batoo, 2011) and electromagnetic interference (EMI) shielding devices. (Gorbachev et al., 2020)

The magnetic properties of Co-Zn ferrites can be enhanced and engineered by the introduction of rare-earth ions into the interstitial sites. These rare-earth ions when placed in the spinel lattice alters structural, electrical, and magnetic properties because of interactions arising between rare-earth and iron ions. (Almuhamady & Aboulfotoh, 2012) Praseodymium substituted Co-Zn ferrites have been reported using ceramic method (Farid et al., 2017).

Bismuth Bi is a diamagnetic element but its doping in the Co-Zn ferrites is reported to yield a promising EMI shielding material (Batoo et al., 2022). It is because of the fact that incorporation of the Bi in place of iron ion changes the saturation magnetization and improvement in electrical properties. (Sharif et al., 2019). Moreover, Bi also modify the structural, magnetic and dielectric properties (Routray, Sanyal, & Behera, 2017) There are no studies available on the Bi and Pr doped Co-Zn spinel ferrites. Among many wet chemical methods Micro-emulsion method is not only simple and economical, but it also gives control and uniformity over particle size. Resulting nanocrystals greatly help in the study of properties of spinel ferrites (Gilani & Shifa, 2018).

The spinel ferrites are used to address several of these issues in the same way as cobalt zinc ferrite (Aubert, Loyau, Mazaleyrat, & LoBue, 2017). There is an abundance of bismuth, cobalt, and zinc. Most zinc is found in minerals. Because they are inexpensive, cobalt, zinc, and bismuth may be employed widely and easily. Regarding these techniques, the practical handling of nanoparticles depends on a variety of factors, including particle size and cation dispersion in the spinel's tetrahedral (A) and octahedral (B) sites (Bharathi & Sankar, 2018). Ferrites also exhibit good dielectric qualities without exhibiting electricity the morally repugnant dielectric features that allow electromagnetic brines to travel through them.

This phenomenon does not arise in the deep earth. Only the ferrites that resemble crystals exhibit dielectric characteristics (Tholkappiyan & Vishista, 2015). Additionally, it has been deduced from the literature that Bi substitution can alter the structural, magnetic, and dielectric properties of ferrites (Routray et al., 2017). The effect of Bi^{2+} substitution on the electrical characteristics of praseodymium cobalt zinc ferrites is explored in this paper. Utilizing the Micro-emulsion technique, samples are prepared. To fulfil the device's integration requirements, the macroemulsion has become crucial. We intended to verify that there is no evidence of the influence of Bi^{2+} doping on $Co_{0.5}Zn_{0.5}Bi_{0.4-x}Pr_{0.1}Fe_{1.5+x}O_4$ at various variations of x = 0.0, 0.1, 0.2, and 0.3 to create a Nanoparticle.

It is extremely effective to add the right additive to increase or improve the grain size in order to produce Bi^{2+} doping on $Co_{0.5}Zn_{0.5}Bi_{0.4-x}Pr_{0.1}Fe_{1.5+x}O_4$ ceramics with low coercivity and high saturation magnetization at temperature. The work that followed was clearly directed at morphological analysis. Ironstone spinel ferrites still include magnetic iron oxide due to their varied characteristics and usage. $Co_{0.5}Zn_{0.5}Bi_{0.4-x}Pr_{0.1}Fe_{1.5+x}O_4$ of the Nano-ferrites were examined for their physical properties using several characterization techniques, including X-ray diffraction (XRD), Fourier Transformation of infrared spectroscopy (FTIR), UV-visible, and scanning electron microscopy (SEM) (scanning electron microscope). The information on the morphology and structure of Nano-ferrites was then confirmed by SEM and XRD. The spinel ferrite's cubic single-phase structure was formed, according to the XRD pattern. The analysis of samples using X-rays was carried out to investigate the structural change that occurred in the samples as a result of the dopant. The morphology is confirmed using a scanning electron microscope. The Fourier transformation verifies how much of each wavelength is absorbed by the sample. The same information can be expressed naturally by Fourier transformation spectroscopy. The end result of this work helps to produce a material with enhanced features.

In this paper, we report the synthesis of $Co_{0.5}Zn_{0.5}Bi_{0.4-x}Pr_{0.1}Fe_{1.5+x}O_4$ spinel ferrite prepared via micro-emulsion method while taking different Bi concentration (x = 0,0.1, 0.2, 0.3 and 0.4). Effects on structural, electrical, optical and morphology properties also studied with the help of different characterization techniques such as X-ray diffraction (XRD), scanning electron microscope (SEM), UV-visible spectroscopy and Fourier transform infrared spectroscopy (FTIR).

2. Experimental Procedures

The Bi replacement $Co_{0.5}Zn_{0.5}Bi_{0.4-x}Pr_{0.1}Fe_{1.5+x}O_4$ is made through micro-emulsion. this series is constructed using the elements below. It uses ferric nitrate nonahydrate, whose chemical formula is $Fe(NO_3)_3.9H_2O$. Iron Nitrate Molar Mass 404 g/mol, (ACS≥98%) Utilized is Bismuth Nitrate Pentahydrate, whose chemical formula is $Bi(NO_3)_3.9H_2O$. Molecular Weight 485.07 g/mol (99 percent Sigma-Aldrich). Hexahydrate of praseodymium

nitrate N_2O_2Pr.6H_2O It uses zinc nitrate hexahydrate, with a molecular weight of 297.49 g/mol (98% Sigma-Aldrich) Hexahydrate of cobalt nitrate. Co $(NO_3)_3$.6H_2O is the chemical reagent's formula. Molar-mass 291.03 g/mol (98% Sigma-Aldrich) 208.98 g/mol of bismuth (99% Sigma-Aldrich) Acetyl-trimethyl-ammonium bromide (CTAB), Molar mass = 364.45 g/mol On a magnetic hot plate set to a temperature of 55 to 60 ^{0}C, the fixed volumes of a solution of metal salts with a concentration of 0.15M were combined and agitated. Aqueous CTAB solution (100ml, 0.45M) was then employed as the surfactant. The pH was then adjusted using NaOH, and it was kept between 11 and 12 throughout the entire solution.

The reaction mixture was stirred for an additional 4-5 hours. As the reaction mixture changed into participants, they were cleaned with deionized water until the pH reached 7. The sample was placed in the oven for drying, where water was converted to vapors at a temperature of 100^{0}C while the components were ground. Then, annealing was done in a temperature-controlled muffle furnace, the Vulcan A-550, for 7 hours at 700 ^{0}C, heating at a rate of 15 ^{0}C/min. The annealed materials were ground into a powder and evaluated using a variety of methods. The Philips 'X'Pert PRO 3040/60 diffract meter with Cu K as the radiation source was used to conduct the powder XRD analysis to learn more about the purity of the synthesized materials. Perkin Elmer spectrometer was used to see the FT-IR spectra in the case of FTIR spectra. To examine the same at room temperature, UV-visible spectroscopy was performed. Using a scanning electron microscope from Japan (SM-6590 LV), the morphology of powders was examined.

3. Results and Discussion

3.1. FTIR (Fourier Transform Infrared Spectroscopy Analysis)

In 1957, the first reasonably priced spectrometer was able to video record an infrared spectrum (Chaimovich, Vaughan, & Westheimer, 1968). The wavelength range that this device covers is 2.5 m to 15 m. A fundamental molecular vibration's highest termed vibration frequency was chosen to fall within the minor wavelength perimeter (Mekebri, Blondina, & Crane, 2009).

The fact that the dispersing element was a prism made from a rock-salt crystal that was ready to solidify at wavelengths higher than around 15 μm a spectral area that came to be known as the rock-salt region made the higher limit necessary. Later devices increased the range to 25 μm (400 cm^{-1}) using potassium bromide prisms (Connes & Connes, 1966). The far-infrared zone, which begins at a wavelength of 50 μm (200 cm^{-1}), was first recognized. At longer wavelengths, it transforms into the microwave region. The FTIR apparent bands support the praseodymium cobalt zinc ferrite's structural integrity. The spinel ferrites' characteristic extensive band in the 550-600 cm^{-1} (v_1) range suggests that metal ions are extending the pulsations to the tetrahedral site, whereas the band at 400-450 cm^{-1} (v_2) is similar to the octahedral site. This collection indicates an uneven (NO^{3-}) extend vibration to go that the remaining nitrate group since the other weak band to research at a heavy frequency is 1384 cm^{-1}. To demonstrate that the hydroxyl group is responsible for the sample investigation, a thorough band analysis in the range 1642-3430 cm^{-1} was initiated. The C-H group is to be stretched inside the other range of 2845-2923 cm^{-1} (Bartick, 2002). In the range of 500 to 4000 c/m, the FTIR spectrum can reveal a lot about the structure and bonding. If there is moisture in the sample and there is no absorption spectra at the wavelengths above 1250 c/m, FTIR will also show an absorption band above 1250 c/m. Due to trapped nitrogen, an FTIR spectral band can be seen at 1300 c/m. At 555 c/m and 445 c/m in the annealed, the absorption band becomes prominent.

The metal oxygen can be seen in the absorption band value of 408-577 cm^{-1}. Nitrate groups are detected in a weak band at 1379 cm^{-1}. It is known that the C-H group is stretching at the absorption band of 2916 cm^{-1}. The hydroxyl group is visible in the peaks near 3417 and 1630.

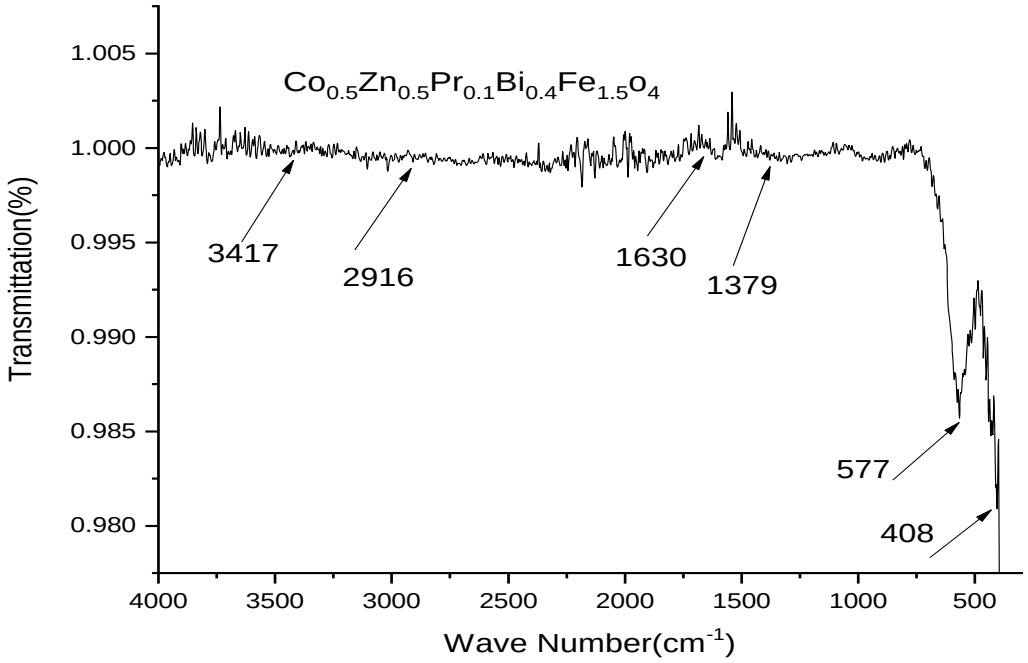

Figure 1: FTIR investigation of $Co_{0.5}Zn_{0.5}Bi_{0.4}Pr_{0.1}Fe_{1.5}O_4$

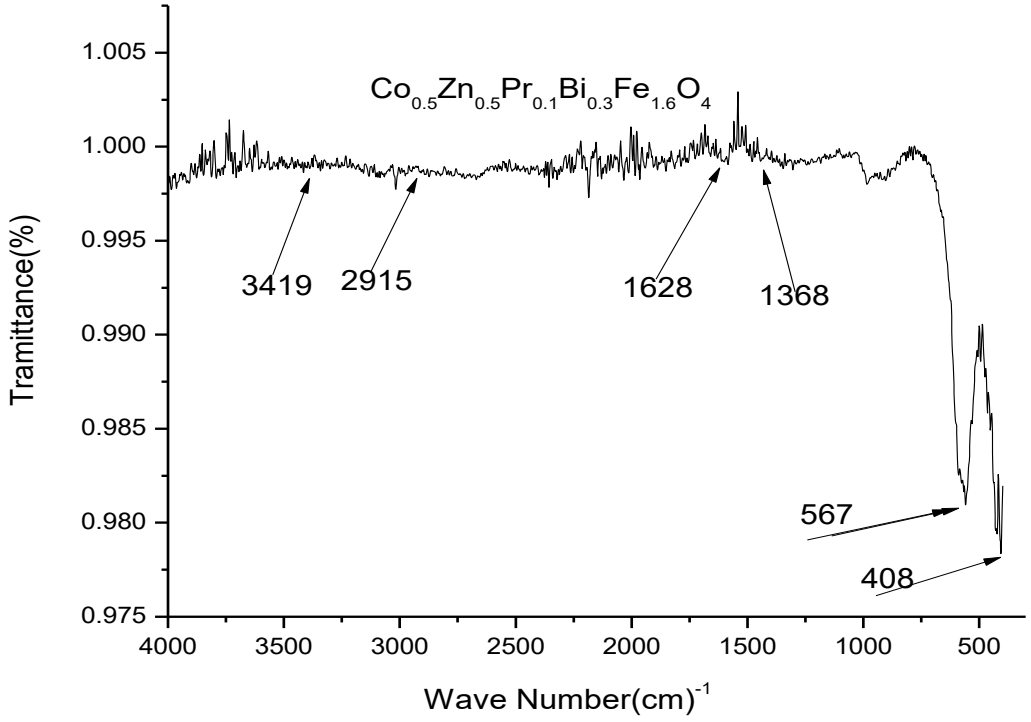

Figure 2: FTIR investigation of $Co_{0.5}Zn_{0.5}Bi_{0.3}Pr_{0.1}Fe_{1.6}O_4$

The metal oxygen may be seen in the absorption band value of 408-567 cm^{-1}. Nitrates are detected in the weak band at 1368 cm^{-1}. It is known that the C-H group is stretching at the absorption band of 2915 cm^{-1}. The hydroxyl group is visible in the peaks between 3419 and 1628.

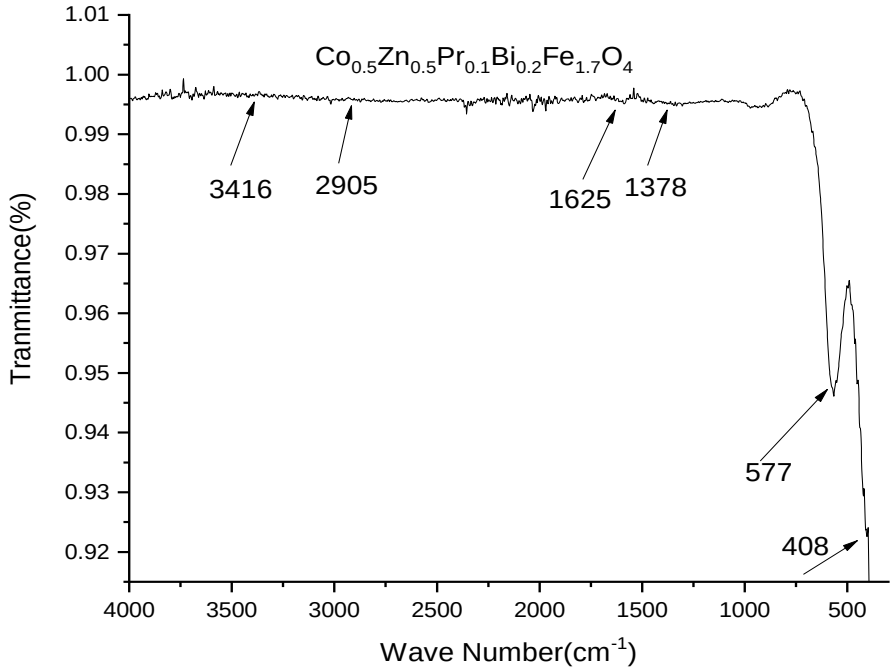

Figure 3: FTIR investigation of $Co_{0.5}Zn_{0.5}Bi_{0.2}Pr_{0.1}Fe_{1.7}O_4$

The metal oxygen can be seen in the absorption band value of 408-577 cm^{-1}. Nitrate groups are detected in a weak band at 1378 cm^{-1}. It is known that the C-H group is stretched in the absorption band at 2905 cm^{-1}. The hydroxyl group is visible in the peaks near 3416 and 1619.

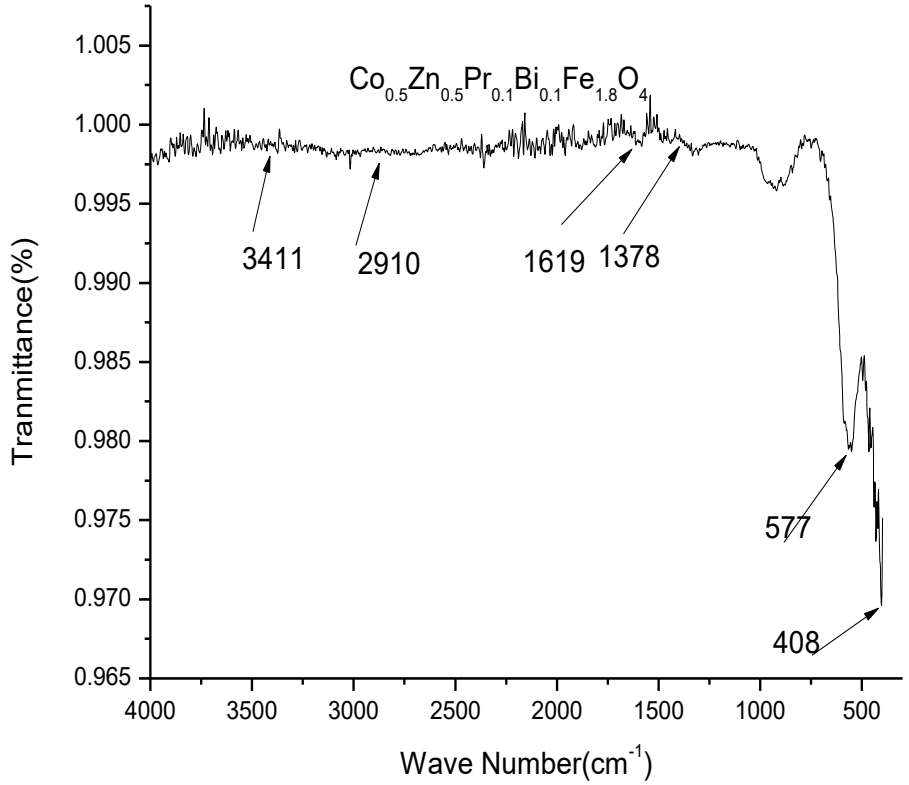

Figure 4: FTIR investigation of $Co_{0.5}Zn_{0.5}Bi_{0.1}Pr_{0.1}Fe_{1.8}O_4$

The metal oxygen can be seen in the absorption band value of 408-577 cm^{-1}. Nitrate groups are detected in a weak band at 1378 cm^{-1}. It is known that the C-H group is stretching at the absorption band of 2910 cm^{-1}. The hydroxyl group is visible in the peaks between 3411 and 1619.

3.2. X-Ray Diffraction Analysis

This method allows us to investigate interplane, distance, crystal size, and crystal. This method also allows us to investigate the parameters of structural lattices. Figures 5 through 8 should show the usual XRD spectra of Bi substituted Pr Co-Zn ferrites with various compositions of x = 0.0, 0.1, 0.2, 0.3, and 0.4. We successfully identified the following peaks as being (111), (200), (220), (311), (222), (400), (422), (511), (440), (620), and (533), which are the distinctive planes of single-phase cubic spinel structure (Bragg & Bragg, 1913) demonstrating the cations' ability to dissolve into the appropriate lattice locations. The crystalline resources can maintain the envoy pattern that continues to be an acceptable source of inquiry in significant sciences by applying X-rays diffracted, or other methods utilizing Bragg's Law (Misra & Dubinskii, 2002). Below is a formula to calculate the lattice constant.

$$a = \frac{\lambda}{2Sin\theta}\sqrt{h^2 + k^2 + l^2} \quad (1)$$

a is the lattice parameters, D is crystalline size, d is inter plane distance, $d_{x\text{-}ray}$ is X-ray density. Lattice constant can be find out with other formula

$$a = d\sqrt{h^2 + k^2 + l^2} \quad (2)$$

$$d = \frac{\lambda}{2Sin\theta} \quad (3)$$

$$D = \frac{K\lambda}{\beta_{hkl} COS\theta} \quad (4)$$

$$d_{x-ray} = \frac{ZM}{N_A V} \quad (5)$$

Here, "h," "k," and "l" stand for the miller index of the given plane, and " λ " denotes the X-ray wavelength. The shape factor is denoted by "k," the unit cell volume is "V," the Bragg's diffraction angle is " θ " the full width at half maxima to the individual plane is "β_{hkl}," the Avogadro's number is "N_A = 6.02 10^{23} g/mol," the molecular mass is "M," and the spinel organization's fragments per unit cell is "Z."

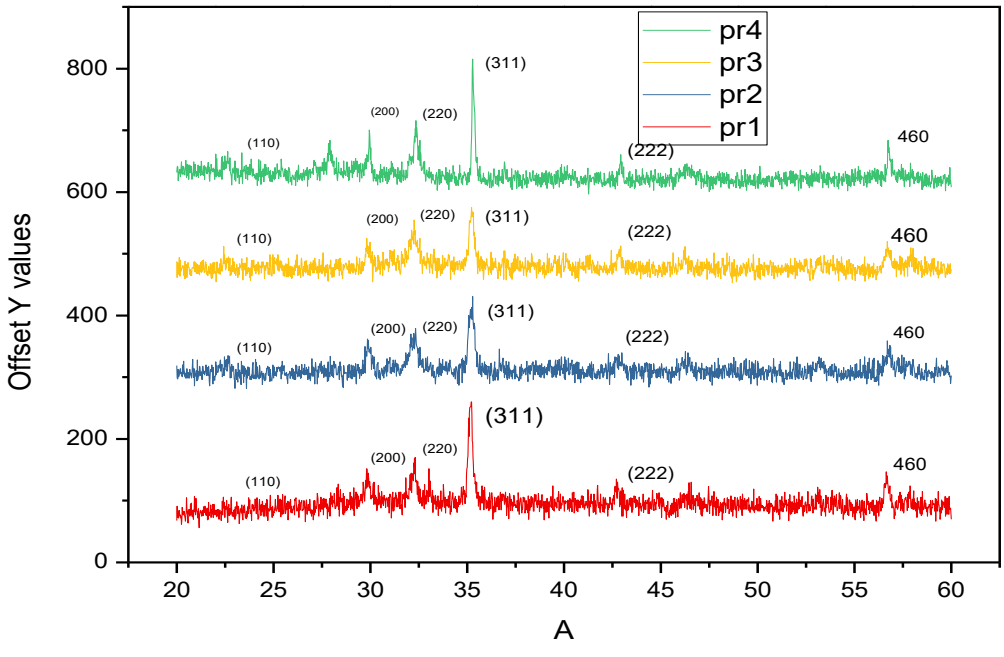

Figure 5: X-Ray Diffraction Analysis of $Co_{0.5}Zn_{0.5}Bi_{0.4-x}Pr_{0.1}Fe_{1.5+x}O_4$

Table 1
Lattice constant, cell volume, Bulk density, X-ray density, and Porosity and Crystalline size of $Co_{0.5}Zn_{0.5}Bi_{0.4-x}Pr_{0.1}Fe_{1.5+x}O_4$

Bi content (x)	X=0.0	X= 0.1	X=0.2	X=0.3
Lattice constant (Å)	8.398	8.396	8.395	8.392
Cell Volume (Å)^3	587.07	586.53	585.32	584.69
Bulk density (g/cm3)	2.53	2.43	2.29	2.21
X-ray density (g/cm^3)	4.85	4.83	4.79	4.76
Porosity	0.49	0.53	0.54	0.55
Crystalline size (nm)	41.09	39.34	35.69	30.69

Bi substituted Co-Zn ferrites crystallize size less than 20 nm and also decreases with increasing the Bi content is reported (Batoo et al., 2022). However in our work larger crystallite size is due to Pr which has larger ionic radii and replacing smaller Fe ion. Pr substituted Co-Zn ferrites crystallize size vary (37.86-50.43) nm, by decreasing Pr content is reported (Farid et al., 2017). In this study crystallize size is found in range of 30 to 41 nm even though Pr and Bi both have been substituted and it is pertinent to mention here that a decreases in crystallize size is observed with increasing Bi content.

3.3. Ultraviolet–Visible Spectroscopy (UV-Vis)

To determine how attentive a test is in a solution, UV-Vis is a quick, easy, and affordable way. It can be used for relatively basic analyses, anywhere the type of compound to be examined (the "analyte") is well-known to conduct a quantitative investigation to confirm the analyte's concentration. Single-beam devices include spectrophotometers. Sample removal is used in single beam devices for measurement. This was the original design, and it is still regularly used in classroom settings and in business laboratories. The UV/Vis spectrophotometer is the name of the device used in ultraviolet-visible spectroscopy (Metha, 2012). It gauges the brightness of light passing through a sample. The ready magnetic nanomaterials on the chart were scanned after the UV-visible analysis was finished. The computation was purposefully consumed by band gap energy in the form of the samples $Co_{0.4}Pr_{0.1}Zn_{0.4}Fe_2O_4$(2.42eV), $Co_{0.4}Pr_{0.1}Zn_{0.4}Bi_{0.05}Fe_{1.95}O_4$ (2.38 eV), $Co_{0.4}Pr_{0.1}Zn_{0.4}Bi_{0.1}Fe_{1.90}O_4$ (2.37eV), and $Co_{0.4}Pr_{0.1}Zn_{0.4}Bi_{0.15}Fe_{1.85}O_4$ (2.32 eV). Since the following equation, the K-M (Kubelka-Munk) model (Suzuki, 2002) and F(R) are commonly used to derive the band gap of these samples from the E_g quantity.

$$F(R) = \frac{(1-R)2}{2R} \quad (6)$$

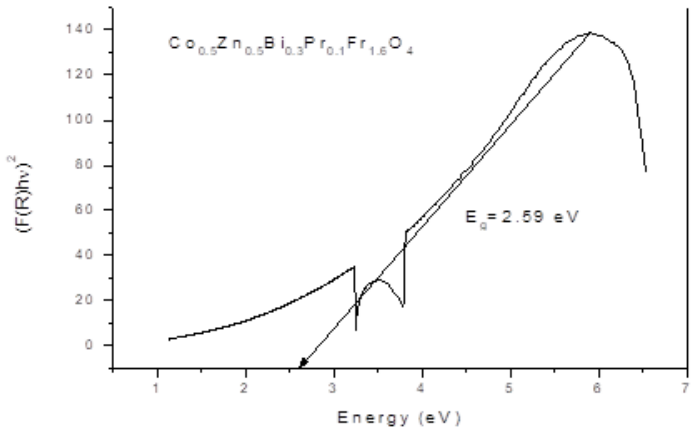

Figure 6: Ultraviolet–visible spectroscopy of $Co_{0.5}Zn_{0.5}Bi_{0.3}Pr_{0.1}Fe_{1.6}O_4$

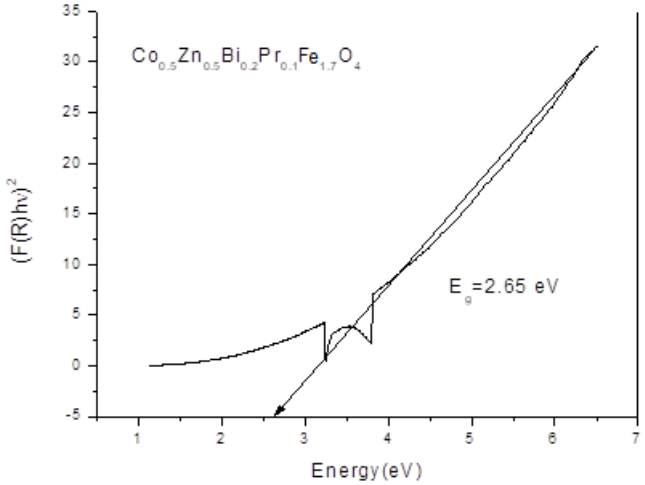

Figure 7: Ultraviolet–visible spectroscopy of $Co_{0.5}Zn_{0.5}Bi_{0.2}Pr_{0.1}Fe_{1.7}O_4$

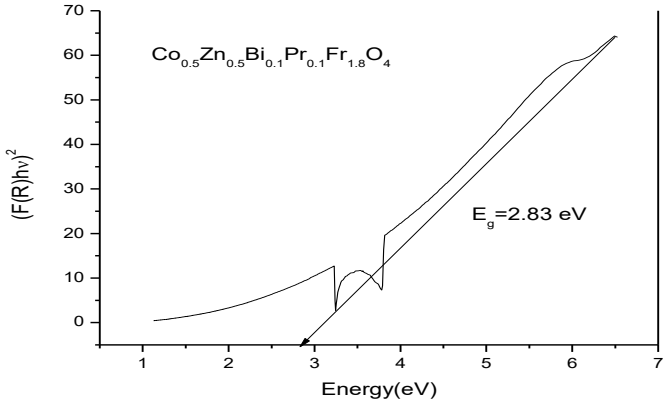

Figure 8: Ultraviolet–visible spectroscopy of $Co_{0.5}Zn_{0.5}Bi_{0.1}Pr_{0.1}Fe_{1.8}O_4$

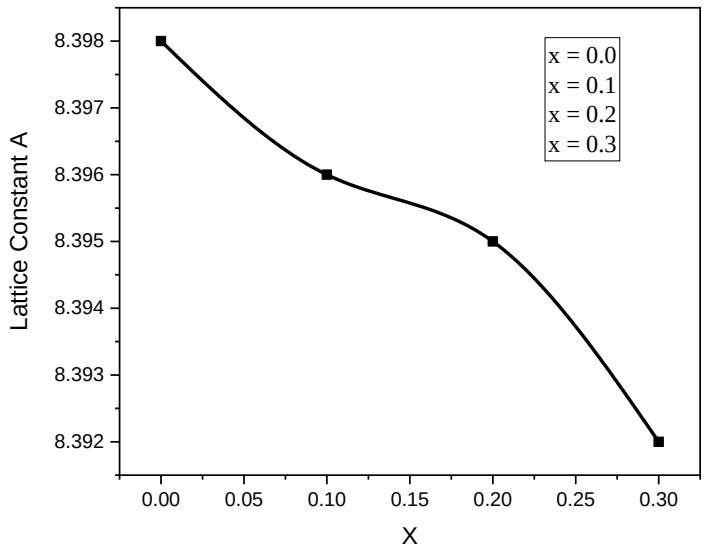

Figure 9: Lattice Constant of $Co_{0.5}Zn_{0.5}Bi_{0.4-x}Pr_{0.1}Fe_{1.5+x}O_4$

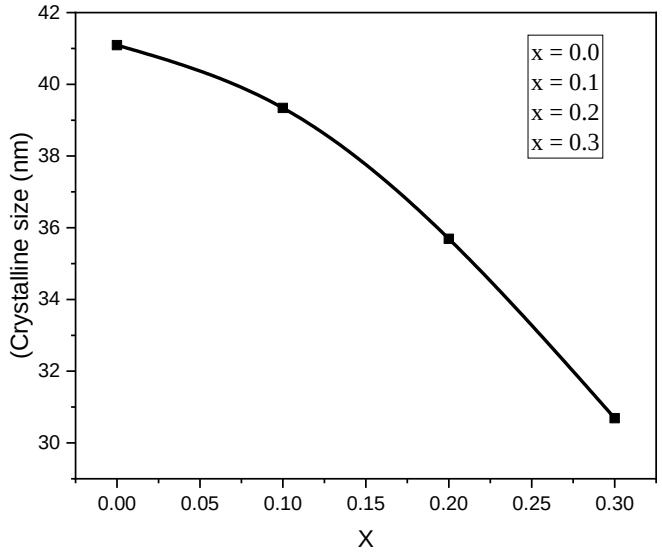

Figure 10: Crystalline size of $Co_{0.5}Zn_{0.5}Bi_{0.4-x}Pr_{0.1}Fe_{1.5+x}O_4$

3.4. Scanning Electron Microscope (SEM)

The scanning electron microscope (SEM) is used to produce a variety of signals at the surface of hard materials using a focused beam of higher-energy electrons (Faulkner, Akman, Bell, Jeffree, & Oparka, 2008). The signals produced by interactions between electrons and samples reveal details on the sample's exterior shape, crystalline structure, chemical composition, and method of material uptake. In the best applications, data are assembled over a selected region of the model's surface, and a 2-dimensional representation of these attributes' spatial changes is created. The traditional (magnification range 20x to 30,000x) SEM techniques can examine areas with widths ranging from around 1 cm to 5 microns (Wergin & Erbe, 1994). The SEM is also unable to conduct studies of selected locations on the sample; this capability is particularly helpful in moulding chemical composition in a qualitative or semi-quantitative manner as well as crystalline structure and crystal orientations. The SEM's goal and function are quite similar to those of the EPMA, and there is a wide range of capabilities shared by the two instruments (Barnes, Mulvaney, Wolff, & Robinson, 2002). When electrons accelerate in a SEM, significant quantities of kinetic energy are consumed, and this energy degenerates as a variety of signals are produced as a result of interactions between the electrons and the sample, as well as when the incident electrons are slowed down in a hard sample. Possibly draining relationship.

$$D = \frac{1.5L}{M \times N} \quad (7)$$

N is the total number of the complete sample, M is the amplification, and L is the overall check line length. The samples' D grain size was abnormal, measuring 41.09 nm. When excited electrons return to lower energy states, they release X-rays with a constant wavelength. As a result, each element in a mineral that the electron beam "excites" emits distinctive X-rays. High-resolution images of the items are created using the SEM, which is also utilized to display spatial differences in the chemical composition. The SEM is also widely used to study single phases that are based on qualitative chemical analysis and sample crystal structure. The SEM can also accurately measure features and objects with a size of 50 nm or smaller (Baghaei, 2007). SEMs equipped with diffracted backscattered electron detection capabilities are used to inspect microfabric. The samples must fit inside the chamber of the microscope and be stable. The largest size in straight dimensions is often between 10 cm and 20 cm, although vertical dimensions are typically much less and almost ever exceed 40 mm. For the majority of devices, samples should be stable in a vacuum between 10^{-5} and 10^{-6} torr. Samples that could outgase at low pressures should not be tested in typical SEMs (Chandler & Roberson, 2009). SEMs feature a wide variety of sample types that can be tested satisfactorily in these specific instruments. SEMs miss light

elements like H, He, and Li, while many instruments miss elements like Na that have atomic numbers below 11. If the device cannot operate in the low vacuum mode, an electrical covering should be helpful to electrically insulate samples for learning about traditional SEMs (Russell & Daghlian, 1985).

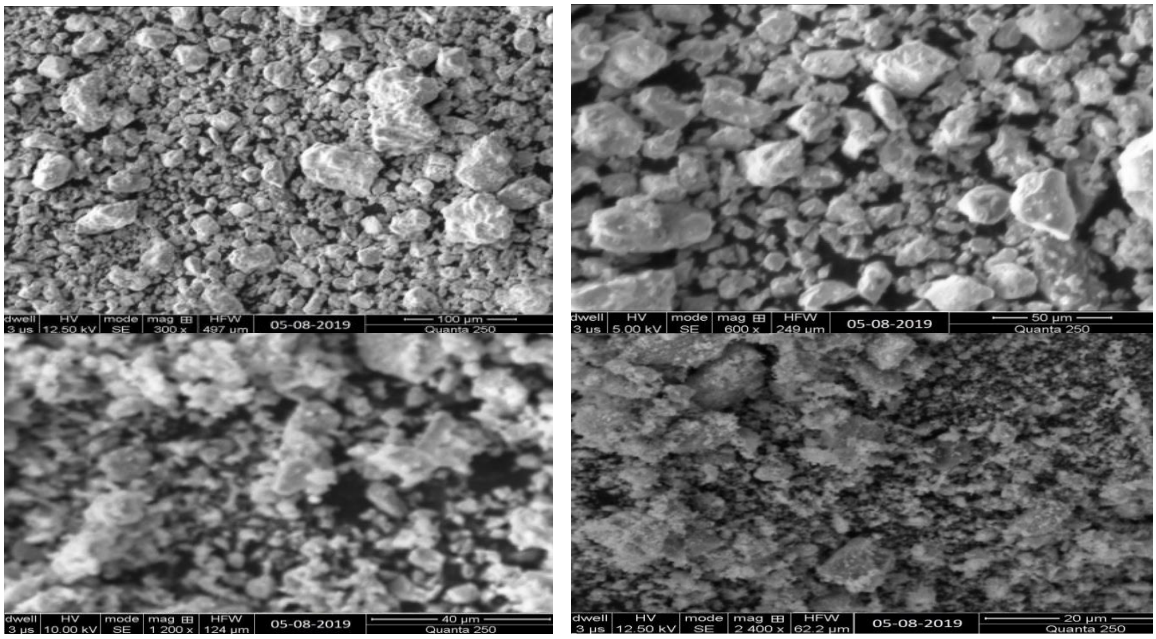

Figure 11: SEM investigation of sample ($Co_{0.5}Zn_{0.5}Bi_{0.4}$ $Pr_{0.1}Fe_{1.5}O_4$)

SEM provides details on the morphology of sample "1" and displays images at various magnifications.

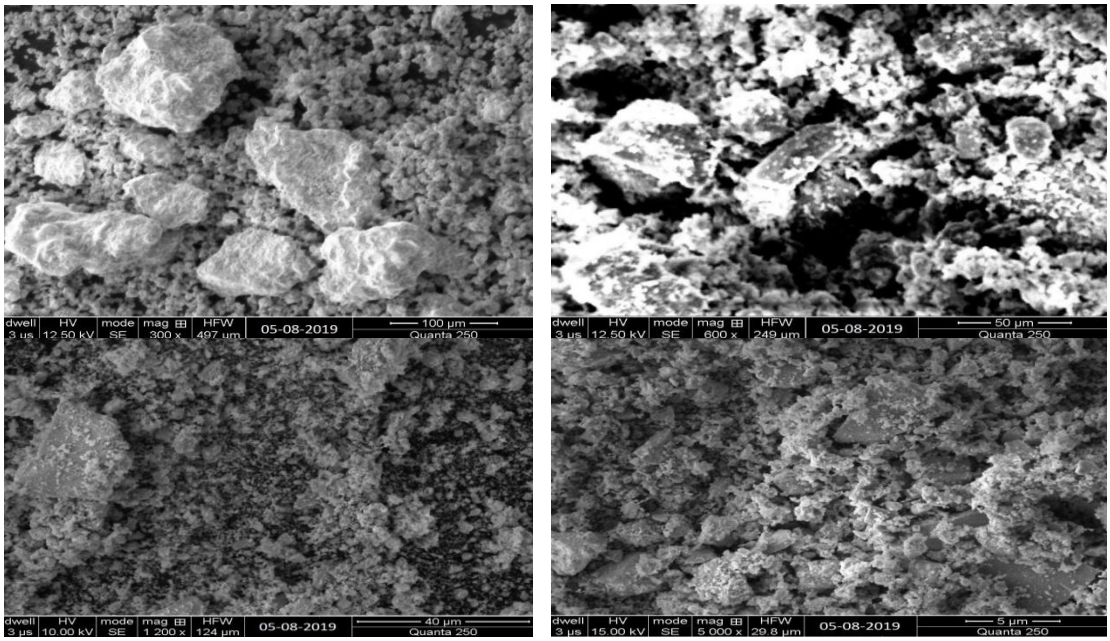

Figure 12: SEM investigation of sample ($Co_{0.5}Zn_{0.5}Bi_{0.3}Pr_{0.1}Fe_{1.6}O_4$)

SEM provides details on the morphology of sample "2" and displays images at various magnifications.

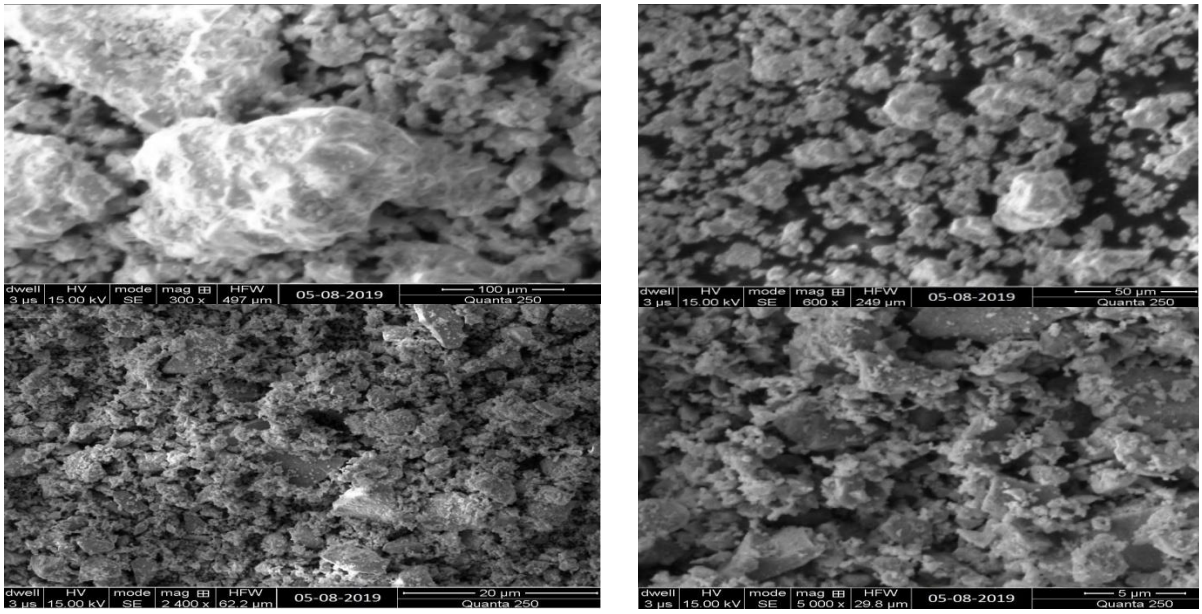

Figure 13: SEM investigation of sample ($Co_{0.5}Zn_{0.5}Bi_{0.2}Pr_{0.1}Fe_{1.7}O_4$)

SEM provides details on the morphology of sample "3" and displays images at various magnifications.

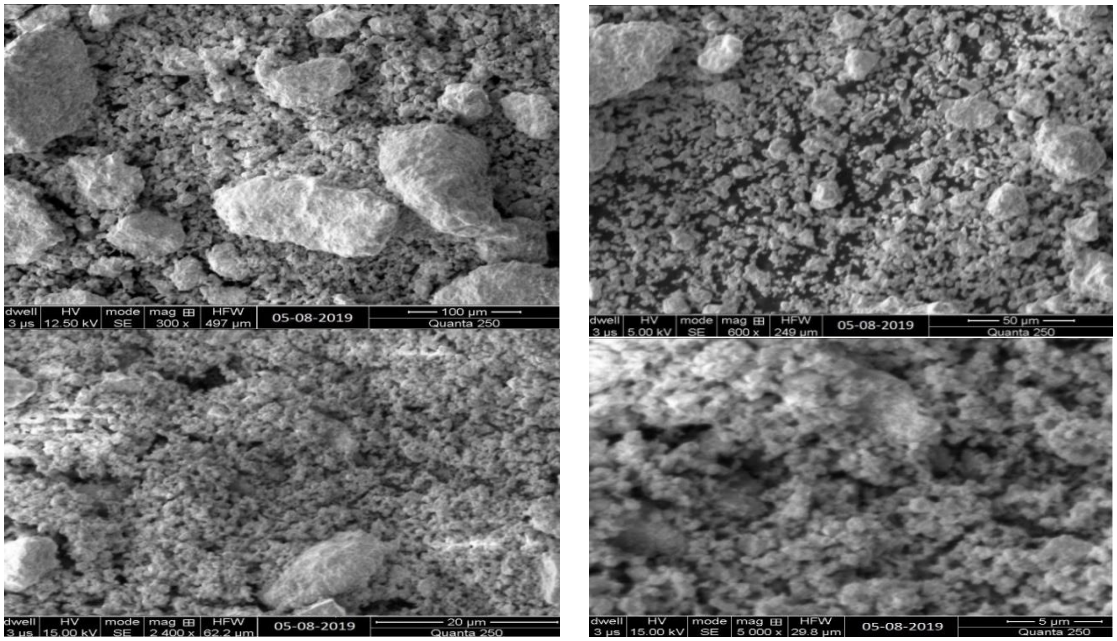

Figure 14: SEM investigation of sample ($Co_{0.5}Zn_{0.5}Bi_{0.1}Pr_{0.1}Fe_{1.8}O_4$)

SEM provides details on the morphology of sample "4" and displays images at various magnifications.

4. Conclusions

We have reported the successful synthesis of $Co_{0.5}Zn_{0.5}Bi_{0.4-x}Pr_{0.1}Fe_{1.5+x}O_4$ spinel ferrite series with varying Bi concentration (x = 0,0.1, 0.2, 0.3 and 0.4) via micro-emulsion method. Spinel structure was confirmed by XRD results. Effects on structural, electrical, optical and morphology properties is studied by varying Bi concentration (x = 0,0.1, 0.2, 0.3 and 0.4). The characterization techniques employed included X-ray diffraction (XRD), Fourier transform infrared spectroscopy, scanning electron microscope (SEM), and UV-visible spectroscopy (FTIR). The spinel structure was verified by XRD measurements to have a lattice parameter of 8.39 Å and particle sizes that increased with increasing Bi concentrations from 30 to 41 nm. The metal oxides band at 408-577 cm^{-1} was identified using Fourier transform infrared spectroscopy (FTIR). Decrease in the value of E_g was

observed from 2.83 eV to 2.59 eV with increase in the Bi content. SEM analysis of the samples' morphology provided this information.

References

Almuhamady, A., & Aboulfotoh, N. (2012). The synthesis and the magnetic properties of Co-Ti Fe2O4 ferrite doped with rare earth ions Nanoparticles. *Journal of American Science, 8*(7), 94-98.

Aubert, A., Loyau, V., Mazaleyrat, F., & LoBue, M. (2017). Uniaxial anisotropy and enhanced magnetostriction of CoFe2O4 induced by reaction under uniaxial pressure with SPS. *Journal of the European Ceramic Society, 37*(9), 3101-3105.

Baghaei, R. (2007). *L.; Computational Scanning Electron Microscopy.* Paper presented at the International Conference on Frontiers of Characterization and Metrology.

Barnes, P., Mulvaney, R., Wolff, E. W., & Robinson, K. (2002). A technique for the examination of polar ice using the scanning electron microscope. *Journal of microscopy, 205*(2), 118-124.

Bartick, E. G. (2002). Applications of vibrational spectroscopy in criminal forensic analysis. *Handbook of vibrational spectroscopy, 4*, 2993-3004.

Batoo, K. M. (2011). Study of dielectric and impedance properties of Mn ferrites. *Physica B: Condensed Matter, 406*(3), 382-387.

Batoo, K. M., Hadi, M., Chauhan, A., Verma, R., Singh, M., Aldossary, O. M., & Bhargava, G. K. (2022). High-frequency applications of bismuth-doped Co–Zn ferrite nanoparticles for electromagnetic interference filter and multilayer inductor chip fabrication. *Applied Physics A, 128*(4), 1-17.

Bharathi, R. N., & Sankar, S. (2018). Effects of transition metal element (Co, Fe, Ni) codoping on structural, optical and magnetic properties of CeO2: Er nanoparticles. *Superlattices and Microstructures, 123*, 37-51.

Bragg, W. H., & Bragg, W. L. (1913). The reflection of X-rays by crystals. *Proceedings of the Royal Society of London. Series A, Containing Papers of a Mathematical and Physical Character, 88*(605), 428-438.

Chaimovich, H., Vaughan, R. J., & Westheimer, F. (1968). Rearrangement accompanying the photolysis of diazoacyl esters. *Journal of the American Chemical Society, 90*(15), 4088-4093.

Chandler, D. E., & Roberson, R. W. (2009). Bioimaging: current concepts in light and electron microscopy.

Connes, J., & Connes, P. (1966). Near-infrared planetary spectra by Fourier spectroscopy. I. Instruments and results. *JOSA, 56*(7), 896-910.

Farid, H. M. T., Ahmad, I., Bhatti, K., Ali, I., Ramay, S. M., & Mahmood, A. (2017). The effect of praseodymium on Cobalt-Zinc spinel ferrites. *Ceramics International, 43*(9), 7253-7260.

Faulkner, C., Akman, O. E., Bell, K., Jeffree, C., & Oparka, K. (2008). Peeking into pit fields: a multiple twinning model of secondary plasmodesmata formation in tobacco. *The Plant Cell, 20*(6), 1504-1518.

Gilani, Z. A., & Shifa, M. S. (2018). HM Noor ul Huda Khan Asghar, Muhammad Azhar Khan, Muhammad Naeem Anjum, Muhammad Nauman Usmani, Rajjab Ali, Muhammad Farooq Warsi, New LiCo0. 5PrxFe2− xO4 nanoferrites: Prepared via low cost technique for high density storage application. *Ceram. Int, 44*, 1881-1885.

Gorbachev, E. A., Trusov, L. A., Sleptsova, A. E., Kozlyakova, E. S., Alyabyeva, L. N., Yegiyan, S. R., . . . Vasiliev, A. V. (2020). Hexaferrite materials displaying ultra-high coercivity and sub-terahertz ferromagnetic resonance frequencies. *Materials Today, 32*, 13-18.

Mekebri, A., Blondina, G., & Crane, D. (2009). Method validation of microcystins in water and tissue by enhanced liquid chromatography tandem mass spectrometry. *Journal of Chromatography a, 1216*(15), 3147-3155.

Metha, A. (2012). Derivation of Beer-Lambert Law. *PharmaXChange. info*.

Misra, P., & Dubinskii, M. A. (2002). *Ultraviolet spectroscopy and UV lasers*: CRC Press.

Routray, K. L., Sanyal, D., & Behera, D. (2017). Dielectric, magnetic, ferroelectric, and Mossbauer properties of bismuth substituted nanosized cobalt ferrites through glycine nitrate synthesis method. *Journal of Applied Physics, 122*(22), 224104.

Russell, S. D., & Daghlian, C. P. (1985). Scanning electron microscopic observations on deembedded biological tissue sections: Comparison of different fixatives and embedding materials. *Journal of Electron Microscopy Technique, 2*(5), 489-495.

Sharif, M., Jacob, J., Javed, M., Manzoor, A., Mahmood, K., & Khan, M. A. (2019). Impact of Co and Mn substitution on structural and dielectric properties of lithium soft ferrites. *Physica B: Condensed Matter, 567*, 45-50.

Suzuki, E. (2002). microscopy of Immunogold-labelled cells by the use of thin plasma coating of Osmium, J . *Microscopy*, 208,153-157.

Tholkappiyan, R., & Vishista, K. (2015). Combustion synthesis of Mg–Er ferrite nanoparticles: cation distribution and structural, optical, and magnetic properties. *Materials Science in Semiconductor Processing, 40*, 631-642.

Velhal, N. B., Patil, N. D., Shelke, A. R., Deshpande, N. G., & Puri, V. R. (2015). Structural, dielectric and magnetic properties of nickel substituted cobalt ferrite nanoparticles: effect of nickel concentration. *AIP Advances, 5*(9), 097166.

Wergin, W., & Erbe, E. (1994). Snow crystals: Capturing snow flakes for observation with the low temperature scanning electron microscope. *Scanning, 16*(17), 1.